also observed at temperatures <100°C. The optimal temperature proved to be 150°C.

We also observed that the reaction rate increased with increasing ethylene pressure. To determine the TOF, we measured TO after 4 hours of reaction. Figure 4 shows a plot of TOF versus ethylene pressure. A linear correlation is observed. Thus, the reaction rate appears to have a first-order dependence on ethylene concentration. This is in contrast to previously reported Pt(II) and Ru(II) catalysts for the hydrophenylation of ethylene, which show an inverse dependence on ethylene pressure (*14*, *17*). For the Pt and Ru catalysts, $M(CH_2CH_2Ph)(\eta^2\text{-}C_2H_4)$ complexes were identified as the likely catalyst resting states. The opposite dependence on ethylene pressure using **1** as catalyst precursor signals a likely change in the catalyst resting state.

To gain further insight into the reaction mechanism, we ran the reaction in a 1:1 molar mixture of C_6H_6 and C_6D_6. After 1 hour, a k_H/k_D (ratio of rate of reaction of protio-benzene and perdeuterobenzene) of 3.1(2) was determined by examining the ratio of undeuterated styrene [mass/charge ratio (m/z) = 104] to styrene-d_5 (m/z = 109) in the mass spectra from three independent experiments (fig. S5). After 2 hours, the observed isotope effect was 3.0(2), statistically equivalent to the data at 1 hour (fig. S5). Thus, the observed k_H/k_D of ~3.1 likely reflects a kinetic isotope effect (KIE) for the catalytic cycle. The KIE is consistent with other transition metal–mediated C–H activation reactions. (*39*, *40*) The primary KIE supports the hypothesis that a Rh catalyst is facilitating a metal-mediated C–H activation process, which occurs before or during the turnover-limiting step. No change in the isotopic distribution for benzene was observed over the course of the reaction, and no styrene-$d_{6\text{-}8}$ products were observed except those predicted by the natural abundance of deuterium in ethylene.

Although more detailed studies are required to understand the reactivity profile of **1**, we believe that the highly electron-withdrawing perfluorophenyl groups on the ^{Fl}DAB ligand help suppress irreversible oxidation to inactive Rh(III) in the presence of Cu(II), possibly facilitate associative ligand exchange between free ethylene and coordinated styrene, and facilitate rapid ethylene insertion into Rh–Ph bonds. Challenges that remain for the continued development of this class of catalyst include increasing activity with the aim of achieving higher conversions of benzene.

REFERENCES AND NOTES

1. G. A. Olah, Á. Molnár, *Hydrocarbon Chemistry* (Wiley, Hoboken, NJ, ed. 2, 2003).
2. C. Perego, P. Pollesel, in *Advances in Nanoporous Materials*, E. Stefan, Ed. (Elsevier, Oxford, 2010), vol. 1, pp. 97–149.
3. S.-S. Chen, in *Kirk-Othmer Encyclopedia of Chemical Technology*, A. Seidel, M. Bickford, Eds. (Wiley, Hoboken, NJ, 2000), pp. 325–357.
4. H. A. Wittcoff, B. G. Reuben, J. S. Plotkin, in *Industrial Organic Chemicals* (Wiley, Hoboken, NJ, 2004), pp. 100–166.
5. Process Evaluation/Research Planning (PERP) Program Report, Styrene/Ethylbenzene, (PERP Report 91-9, Chem Systems, Inc., New York, 1992).
6. M. Lucchini, A. Galeotti, "Improved process for the dehydrogenation of alkyl-aromatic hydrocarbons for the production of vinyl-aromatic monomers" (International Patent WO2007073918A1, 2007).
7. C. Perego, P. Ingallina, *Catal. Today* **73**, 3–22 (2002).
8. C. Perego, P. Ingallina, *Green Chem.* **6**, 274 (2004).
9. J. Čejka, B. Wichterlová, *Catal. Rev.* **44**, 375–421 (2002).
10. I. M. Gerzeliev, S. N. Khadzhiev, I. E. Sakharova, *Petrol. Chem.* **51**, 39–48 (2011).
11. *CRC Handbook of Chemistry and Physics* (CRC Press, Boca Raton, FL, 1977).
12. M. Lail, B. N. Arrowood, T. B. Gunnoe, *J. Am. Chem. Soc.* **125**, 7506–7507 (2003).
13. M. Lail *et al.*, *Organometallics* **23**, 5007–5020 (2004).
14. N. A. Foley, J. P. Lee, Z. Ke, T. B. Gunnoe, T. R. Cundari, *Acc. Chem. Res.* **42**, 585–597 (2009).
15. E. E. Joslin *et al.*, *Organometallics* **31**, 6851–6860 (2012).
16. J. R. Andreatta, B. A. McKeown, T. B. Gunnoe, *J. Organomet. Chem.* **696**, 305–315 (2011).
17. B. A. McKeown *et al.*, *J. Am. Chem. Soc.* **133**, 19131–19152 (2011).
18. B. A. McKeown, H. E. Gonzalez, T. B. Gunnoe, T. R. Cundari, M. Sabat, *ACS Catal.* **3**, 1165–1171 (2013).
19. B. A. McKeown, B. M. Prince, Z. Ramiro, T. B. Gunnoe, T. R. Cundari, *ACS Catal.* **4**, 1607–1615 (2014).
20. S. A. Burgess *et al.*, *Chem. Sci.* **5**, 4355–4366 (2014).
21. W. D. Jones, J. A. Maguire, G. P. Rosini, *Inorg. Chim. Acta* **270**, 77–86 (1998).
22. A. T. Luedtke, K. I. Goldberg, *Angew. Chem. Int. Ed.* **47**, 7694–7696 (2008).
23. T. Matsumoto, D. J. Taube, R. A. Periana, H. Taube, H. Yoshida, *J. Am. Chem. Soc.* **122**, 7414–7415 (2000).
24. T. Matsumoto, R. A. Periana, D. J. Taube, H. Yoshida, *J. Mol. Catal. A* **180**, 1–18 (2002).
25. J. Oxgaard, R. P. Muller, W. A. Goddard 3rd, R. A. Periana, *J. Am. Chem. Soc.* **126**, 352–363 (2004).
26. B. A. McKeown, N. A. Foley, J. P. Lee, T. B. Gunnoe, *Organometallics* **27**, 4031–4033 (2008).
27. B. A. McKeown *et al.*, *Organometallics* **32**, 3903–3913 (2013).
28. B. A. McKeown *et al.*, *Organometallics* **32**, 2857–2865 (2013).
29. P. Hong, H. Yamazaki, *J. Mol. Catal.* **26**, 297–311 (1984).
30. D. Taube, R. Periana, T. Matsumoto, "Oxidative coupling of olefins and aromatics using a rhodium catalyst and a copper(II) redox agent" (U.S. Patent 6127590A, 2000).
31. Y. Fujiwara, I. Noritani, S. Danno, R. Asano, S. Teranishi, *J. Am. Chem. Soc.* **91**, 7166–7169 (1969).
32. T. Yamada, A. Sakakura, S. Sakaguchi, Y. Obora, Y. Ishii, *New J. Chem.* **32**, 738 (2008).
33. A. Kubota, M. H. Emmert, M. S. Sanford, *Org. Lett.* **14**, 1760–1763 (2012).
34. K. Sasaki, T. Sakakura, Y. Tokunaga, K. Wada, M. Tanaka, *Chem. Lett.* **17**, 685–688 (1988).
35. American Chemical Society, *Chem. Eng. News Archive* **39** (16), 52–55 (1961).
36. W. A. Herrmann, in *Catalysis from A to Z*, B. Cornils, W. A. Herrmann, M. Muhler, C.-H. Wong, Eds. (Wiley, Weinheim, Germany, 2007), pp. 1512–1524.
37. M. Eckert, G. Fleischmann, R. Jira, H. M. Bolt, K. Golka, in *Ullmann's Encyclopedia of Industrial Chemistry* (Wiley-VCH Verlag, Weinheim, Germany, 2000), pp. 1–17.
38. M. S. Webster-Gardiner *et al.*, *Cat. Sci. Tech.* **5**, 96–100 (2015).
39. M. Gómez-Gallego, M. A. Sierra, *Chem. Rev.* **111**, 4857–4963 (2011).
40. W. D. Jones, *Acc. Chem. Res.* **36**, 140–146 (2003).

ACKNOWLEDGMENTS

The authors acknowledge support from the U.S. Department of Energy, Office of Basic Energy Sciences [DE-SC0000776 (T.B.G.) and DE-FG02-03ER15387 (T.R.C.)] for studies of styrene catalysis; the Center for Catalytic Hydrocarbon Functionalization, an Energy Frontier Research Center (award DE-SC0001298), which funded the initial catalyst discovery; and an AES Corporation Graduate Fellowship in Energy Research (M.S.W.-G). The authors also thank B. McKeown, G. Fortman, S. Kalman (University of Virginia), and R. Nielsen (California Institute of Technology) for helpful discussions.

SUPPLEMENTARY MATERIALS

www.sciencemag.org/content/348/6233/421/suppl/DC1
Materials and Methods
Figs. S1 to S4
Table S1
References (*41*–*43*)

3 November 2014; accepted 12 March 2015
10.1126/science.aaa2260

SELF-ASSEMBLY

Selective assemblies of giant tetrahedra via precisely controlled positional interactions

Mingjun Huang,[1] Chih-Hao Hsu,[1] Jing Wang,[1] Shan Mei,[1] Xuehui Dong,[1] Yiwen Li,[1] Mingxuan Li,[1] Hao Liu,[1] Wei Zhang,[1] Takuzo Aida,[2] Wen-Bin Zhang,[3]* Kan Yue,[1]* Stephen Z. D. Cheng[1]*

Self-assembly of rigid building blocks with explicit shape and symmetry is substantially influenced by the geometric factors and remains largely unexplored. We report the selective assembly behaviors of a class of precisely defined, nanosized giant tetrahedra constructed by placing different polyhedral oligomeric silsesquioxane (POSS) molecular nanoparticles at the vertices of a rigid tetrahedral framework. Designed symmetry breaking of these giant tetrahedra introduces precise positional interactions and results in diverse selectively assembled, highly ordered supramolecular lattices including a Frank-Kasper A15 phase, which resembles the essential structural features of certain metal alloys but at a larger length scale. These results demonstrate the power of persistent molecular geometry with balanced enthalpy and entropy in creating thermodynamically stable supramolecular lattices with properties distinct from those of other self-assembling soft materials.

Self-assembled hierarchical structures in soft materials have been intensely studied. Among them, assemblies of building blocks with specific geometric shapes and symmetry are of particular interest. As the simplest case, ordered structures constructed from packing of spherical motifs have been a classic yet dynamic research field that can be traced back to the study of metals and metal alloys. Most metal atoms, viewed as congruent spheres, typically tend

to hold 12 neighbors (the coordination number, CN, is thus 12) in local environments, forming the most efficient packing scheme with tetrahedral interstices (*1*). This type of structure allows three possible variations: face-centered cubic (the cuboctahedron), hexagonal close-packed (the twinned cuboctahedron), and the topologically close-packed icosahedron (or "icosahedral coordination").

In metal alloys, different metal atoms with various sizes and electronic states are involved. Frank and Kasper (*2*) studied the stability of icosahedral lattices and proved that distorted icosahedra could be accommodated with topologically close-packed Kasper polyhedra, which allow even higher coordination numbers (CN = 14, 15, and 16) in metal alloy crystals. This class of metal alloy crystal structures is referred as the "Frank-Kasper" phases, including the A15 phase (with an A_3B stoichiometry such as Cr_3Si), the Friauf-Laves phase (with an A_2B stoichiometry such as Zn_2Mg), the σ phase (with an AB stoichiometry such as CrFe), and others (*3*). Some Frank-Kasper phases are viewed as periodic approximates of aperiodic "quasicrystals." Therefore, they provide a platform to understand how to fill in space with different spherical motifs and how to achieve properties related to their characteristic structural features of low lattice symmetry and high coordination numbers.

A typical cubic unit cell of the A15 phase (Fig. 1A) consists of six A units (pale red spheres) in 14-fold Kasper polyhedra and two B units (dark red spheres) in 12-fold icosahedral coordination (Fig. 1B) with a space group of $Pm\bar{3}n$ (O_h^3). The projection view along the ⟨001⟩ direction (Fig. 1C) displays a regular two-dimensional (2D) 4^4 tiling pattern (*4*). Recently, examples of the A15, σ, and quasicrystalline phases constructed by nano- and micrometer-sized "deformable" spheres, micelles, and colloids were reported in many systems, including spherical dendrimers (*5*–*8*), ABC star-triblock copolymers (*9*), micelles of linear diblock or tetrablock copolymers in the bulk (*10*–*12*) or in solution (*13*), binary nanoparticle lattices (*14*), and mesoporous silica produced from surfactant micelles (*15*). In particular, formation of the A15 phase in dendrimers has been attributed to the presence of soft "squishy surface layers" composed of alkyl chains, which can deform to minimize steric interactions (*5*, *16*) and surface contact area among the spheres (the Weaire-Phelan structure) (*17*, *18*).

Constructing ordered phases with the use of shaped building blocks other than spheres has yet to be demonstrated. Recent computer simulation results revealed possible crystalline and liquid crystalline structures from the packing of polyhedra (*19*). Among all the polyhedra, the tetrahedron is the simplest. Rigid tetrahedron building blocks have been shown to form quasicrystalline and crystalline phases with high packing fractions (*20*). However, related experimental investigation remains largely unexplored in terms of both observations of ordered structures and their formation mechanisms. Shape-persistent molecular nanoparticles, such as derivatives of POSS (*21*), fullerenes (*22*), polyoxometalates (*23*), and proteins (*24*), offer great opportunities to construct nanosized giant tetrahedra with atomic precision (*25*, *26*).

Here, we present an experimental study of giant tetrahedra constructed by attaching four POSS cages with different functional groups to a rigid tetrahedral core (Fig. 2). They are distinguished from the reported dendrimer and block copolymer systems (*12*) by the absence of any flexible alkyl or polymeric chains. Self-assembly of these giant tetrahedra is mediated by interactions among the POSS nanoclusters and the

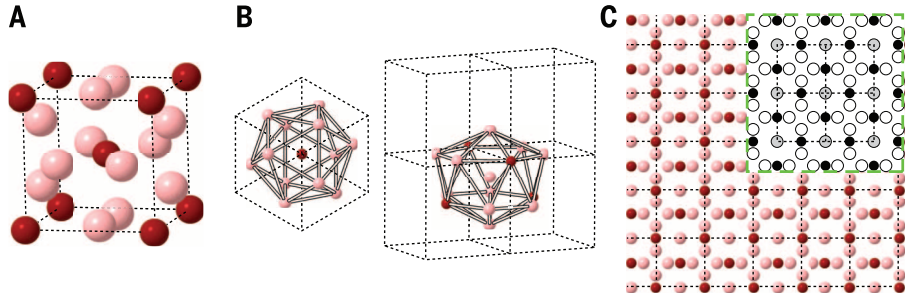

Fig. 1. Schematic illustration of the A15 phase. (**A**) In an A15 cubic unit cell, the dark red and pale red colors represent different coordination environments. (**B**) Schemes of CN = 12 and CN = 14 coordination environments in the A15 lattice. (**C**) 2D-projected view of the A15 lattice along the ⟨001⟩ direction. The inset shows a 2D 4^4 tiling pattern along the z axis. The spheres at the sparse layers (z/4 and 3z/4) are represented by gray circles; the spheres at the dense layers are shown by black and white circles (z/2 and z).

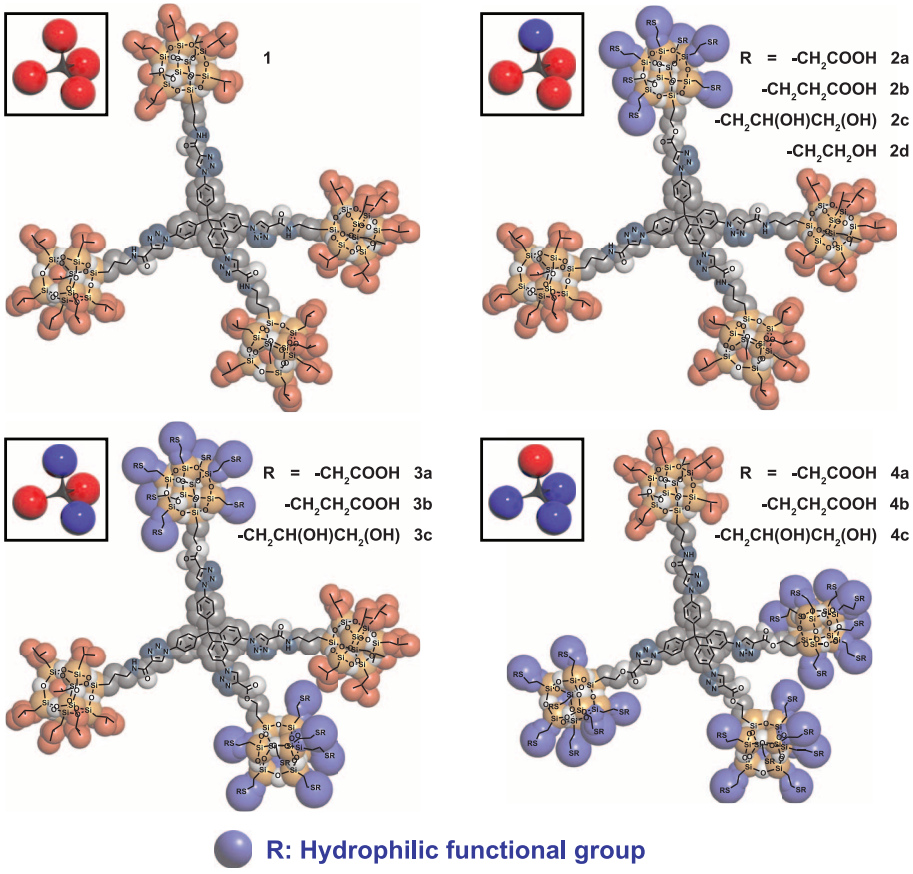

Fig. 2. Chemical structures and molecular models (shown in shadow) of the four categories of giant tetrahedra. Cartoons in the boxes are corresponding simplifications of the giant tetrahedra, in which blue spheres represent hydrophilic POSS cages and red spheres represent hydrophobic BPOSS cages.

[1]Department of Polymer Science, College of Polymer Science and Polymer Engineering, University of Akron, Akron, OH 44325, USA. [2]Department of Chemistry and Biotechnology, School of Engineering, University of Tokyo, 7-3-1 Hongo, Bunkyo-ku, Tokyo 113-8656, Japan. [3]Key Laboratory of Polymer Chemistry and Physics of Ministry of Education, Center for Soft Matter Science and Engineering, College of Chemistry and Molecular Engineering, Peking University, Beijing 100871, P.R. China.
***Corresponding author. E-mail: scheng@uakron.edu (S.Z.D.C.); ky13@zips.uakron.edu (K.Y.); wenbin@pku.edu.cn (W.-B.Z.)**

overall molecular symmetry. Various ordered supramolecular lattices, including the Frank-Kasper A15 phase, are observed in this system by tuning the numbers of hydrophilic or hydrophobic POSS cages in each molecule and the functional groups on the hydrophilic POSS cages.

Giant tetrahedra **1** to **4** with different partitions of hydrophobic and hydrophilic POSS cages were synthesized by sequentially applying two "click" reactions (fig. S1): the copper-catalyzed azide-alkyne [3+2] cycloaddition reaction and the thiol-ene reaction (*27*, *28*). The hydrophobic POSS cages have seven isobutyl groups (BPOSS) and the hydrophilic POSS cages have either hydroxyl or carboxylic acid groups (Fig. 2). Incorporation of different POSS cages results in competing interactions (i.e., collective hydrogen-bonding interactions among the hydrophilic POSS cages and the crystallization of BPOSS cages) to drive self-assembly; tuning the number of hydrophobic or hydrophilic POSS cages systematically varies molecular symmetry of the giant tetrahedra. Nuclear magnetic resonance and mass spectroscopy results (figs. S2 and S3) confirmed their structural precision and high purity. We expect that geometric and interactional factors jointly determine their self-assembly behaviors.

Giant tetrahedron **1** contains four identical BPOSS cages. A crystalline structure with a triclinic unit cell and a space group of *P1* has been determined (fig. S4 and table S1), based on the combination of selected-area electron diffraction (SAED; fig. S4A) data from its single crystals and wide-angle x-ray diffraction (WAXD; fig. S4B) data from the bulk sample (*28*). In the simulated molecular packing, the tetrahedral cores adopt an interpenetrated stacking manner to form geometrically locked columns, which are surrounded by a shell of crystalline BPOSS cages (fig. S4, D and E). To maximize the contacts among the crystalline BPOSS cages, the lattice is distorted from hexagonally packed cylinders toward lower symmetry.

Replacing one BPOSS cage with a hydrophilic POSS cage in **1** lowers the molecular symmetry to *C3v* and results in giant tetrahedra **2a** to **2c**. At 25°C, density-frustrated lamellar supramolecular structures with a three-layer packing periodicity are observed in **2a** to **2c**, as supported by the combined small-angle x-ray scattering (SAXS) and WAXD results (Fig. 3A) with a scattering vector (q) value ratio of 1:2:3. Besides, the strongest diffraction peak at 1.09 nm in the WAXD pattern is attributed to the characteristic diffraction of crystalline BPOSS domains (*29*). A bright-field (BF) transmission electron microscope (TEM) image of microtomed thin-sectioned **2a** samples (Fig. 3B) and its fast Fourier transform (FFT) pattern (Fig. 3B, inset) also confirm the lamellar structure. The measured periodicities of 4.3 to 4.7 nm (Table 1) can only accommodate two layers of BPOSS and one interdigitated layer of the hydrophilic POSS cages (Fig. 3G) (estimated ~4.5 nm). Despite the unmatched numbers of hydrophobic and hydrophilic POSS cages, crystallization of BPOSS cages dominates and preferentially creates flat interfaces (*30*), leading to the formation of frustrated supramolecular lamellae.

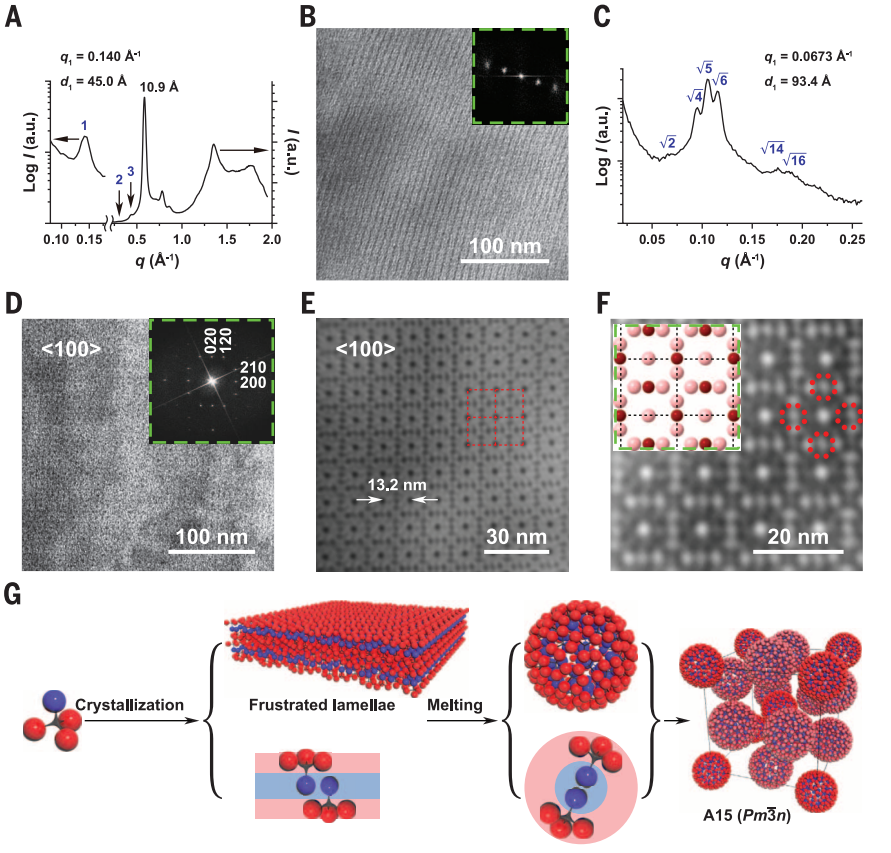

Fig. 3. Selectively assembled structures of 2a. (**A**) Combined SAXS and WAXD profiles of **2a** evaporated from tetrahydrofuran-acetonitrile (THF/MeCN) mixed solvents at 25°C. (**B**) BF TEM image and corresponding FFT pattern (inset) of a microtomed thin-sectioned **2a** sample. (**C**) SAXS pattern of **2a** after the sample was heated to above its T_m and annealed at 140°C for 12 hours. (**D**) A {100} plane of an A15 supramolecular lattice was identified by the BF TEM image after the thin-sectioned sample was stained by RuO_4. The inset is the FFT pattern of this image. (**E**) Fourier filtering of the image shown in (D) revealed a clear view of the 2D 4^4 tiling along the ⟨100⟩ direction. (**F**) Inverse colored and magnified image of (E). White spheres represent the hydrophilic POSS domains with different sizes. The inset shows a simulated projection view along the ⟨100⟩ direction. Spheres in the red-dot circles correspond to the dark red ones shown in Fig. 1A. (**G**) Schematic illustrations of the selective assembly mechanism and molecular packing in the A15 lattice.

Table 1. Supramolecular lattice analysis of the giant tetrahedra with different symmetry. Lattice I structures were formed by slow evaporation of the sample solutions in THF/MeCN mixed solvents at 25°C; lattice II structures were formed after annealing treatment. d_I is the determined periodicity of the lamellar structures.

Molecule	Lattice I	T_m (°C)	d_I (nm)	Lattice II	d_{II} (nm)	M
1	Triclinic crystal	138	—	Disordered	—	—
2a	Lamellae	145	4.50	A15	13.2*	38/50§
2b	Lamellae	144	4.60	A15	14.2*	46/61§
2c	Lamellae	146	4.67	A15	14.6*	49/65§
2d	Lamellae	126	4.50	bcc	8.2*	44§
3a	Lamellae	177	5.40	Double gyroid	6.35	—
3b	Lamellae	172	5.90	Lamellae	6.40†	—
3c	Lamellae	180	6.00	Lamellae	7.30†	—
4a	Disordered	—	—	Cylinder	6.22‡	6.7#
4b	Disordered	—	—	Cylinder	6.28‡	6.6#
4c	Disordered	—	—	Cylinder	6.70‡	7.4#

*Dimensions of the A15 or bcc unit cells. †Lamellar periodicities in supramolecular lattice II. ‡The corresponding principal (01) spacing between the cylinders in the honeycomb-like hexagonal lattices. §Calculated numbers of giant tetrahedra in two types of spheres in the A15 lattice (the size ratios of two types of spheres in **2b** and **2c** are assumed to be 1.1, the same as in **2a**) or in each sphere in the bcc lattice. #Average number of giant tetrahedra within 1-nm-thick cross section of the cylinders in the honeycomb-like hexagonal supramolecular lattices.

After **2a** was heated to 180°C (above its melting point T_m; Table 1) and immediately cooled to and annealed at 140°C for 12 hours, an entirely different SAXS pattern was observed (Fig. 3C). The WAXD pattern indicates that BPOSS cages were amorphous in this structure (fig. S5A). Both **2b** and **2c** exhibited virtually identical SAXS patterns upon the same thermal treatment (fig. S5, B and C). The observed q value ratios (Fig. 2C and fig. S5, B and C) are $\sqrt{2}:\sqrt{4}:\sqrt{5}:\sqrt{6}$, which is characteristic of the A15 phase (*5*). A cubic unit cell with a = 13.2 nm can be deduced for **2a**. The lattice assignment is further validated by TEM images of the microtomed, RuO_4-stained thin-sectioned samples of **2a** (~80 nm thick). The BF TEM image in Fig. 3D exhibits the arrangement of spheres along the ⟨100⟩ direction of the A15 phase in real space. Its FFT pattern is shown in the inset of Fig. 3D (also in fig. S5D) with major diffractions assigned. Fourier filtering treatment provides a clear view of the regular 2D 4^4 tiling pattern along the ⟨100⟩ direction (Fig. 3E). From this image, the measured distance between two closest neighboring squares is 13.2 nm, which is consistent with the value calculated from the SAXS result. Setting Fig. 3E in inverse contrast makes it easier to identify the fine features of the spherical packing (Fig. 3F). It is observed that spheres in the red-dot circles (Fig. 3F), which correspond to the dark red spheres in Fig. 1A with CN = 12, are smaller relative to their neighbors (pale red spheres in Fig. 1A with CN = 14). On the basis of the average size ratio between these two types of spheres (1.1 ± 0.06), we estimate that these two types of spheres contain 38 and 50 giant tetrahedra, respectively (*28*). These results support the existence of two types of spheres with different coordination environments in a single-component system, in contrast to metal alloys with different types of atoms. Moreover, the number of giant tetrahedra in each sphere is found to increase with increasing strength of the collective hydrogen-bonding interactions and the molecular masses from **2a** to **2c** (Table 1). The formation mechanism of the A15 phase is illustrated in Fig. 3G. When the frustrated lamellar crystals melt, the hydrophilic POSS cages form spherical aggregates via collective hydrogen bonding, while BPOSS cages originally located in the neighboring top and bottom lamellar layers undergo a 2D scrolling to form the shell. The self-assembled spheres finally pack into the A15 supramolecular lattice.

Dendrimers with a poly(benzyl ether) core and a dodecyl corona are known to form spheres that further pack into A15 lattices (*5*, *7*), which can be explained by the soft "squishy surface layers" that promote deformation of the spheres to maximize entropy and minimize interfaces (*17*, *18*, *31*, *32*). The molecular geometry of giant tetrahedra **2a** to **2c** also prefers the formation of spheres in the first step. Without any flexible chains, it is proposed that extra degrees of freedom (such as the excluded volume of BPOSS cages and the nonclose packing of the hydrophilic POSS cages via hydrogen bonding) contribute to the size differentiations of the assembled spherical motifs, which entropically favor more space and looser packing to form the A15 phase. Furthermore, it is believed that the deformability is associated with the size of the spheres, because the interstitial gaps become larger as the size of spheres increases (*16*).

To prove this assumption, we synthesized **2d** (Fig. 2 and fig. S6A) containing a hydrophilic POSS cage with the weakest hydrogen-bonding interaction and the smallest molar mass among **2a** to **2d**. After similar thermal treatment, a body-centered cubic (bcc) lattice composed of only one type of spheres was found (fig. S6). Each sphere contains 44 giant tetrahedra **2d**. This number provides a reasonable estimation of the upper size limit of nondeformable spheres assembled from this series of giant tetrahedra, because a small fraction of the A15 phase can also be identified from the TEM image of thin-sectioned **2d** samples (fig. S6F). Any spheres larger than this size would deform as the result of nonclose packing of the hydrophilic POSS cages at the spherical center (*33*) to better fit into the supramolecular lattice-packing requirements with lower symmetry.

Giant tetrahedra **3a** to **3c** are more symmetric in terms of both volume fractions and interactions. "Double-layered" lamellar supramolecular lattices (*30*, *34*) are observed for **3a** to **3c** at 25°C, due to the dominating BPOSS crystallization (fig. S7A). Layer thicknesses of these lamellar structures were determined from SAXS results (Table 1 and fig. S7B), and they match the estimated values from molecular packing models (*28*). Their high-temperature structures were obtained by annealing above their T_m at 180°C for 3 hours and subsequent quenching into liquid nitrogen to suppress crystallization of BPOSS cages (fig. S7C). SAXS and TEM results (Fig. 4, A and D) indicate that the lamellar structures of **3b** and **3c** remain but have increased lamellae d-spacings relative to their room-temperature structures; this is mainly attributed to the disordered BPOSS packing and thermal expansion. On the other hand, a highly ordered double-gyroid supramolecular lattice (space group $Ia\bar{3}d$) forms in **3a** after similar treatment (Fig. 4, B and E, and fig. S7D). In the TEM image (Fig. 4E), the darker regions are hydrophilic POSS domains embedded in the hydrophobic matrix composed of BPOSS cages and the tetrahedral cores. Formation of

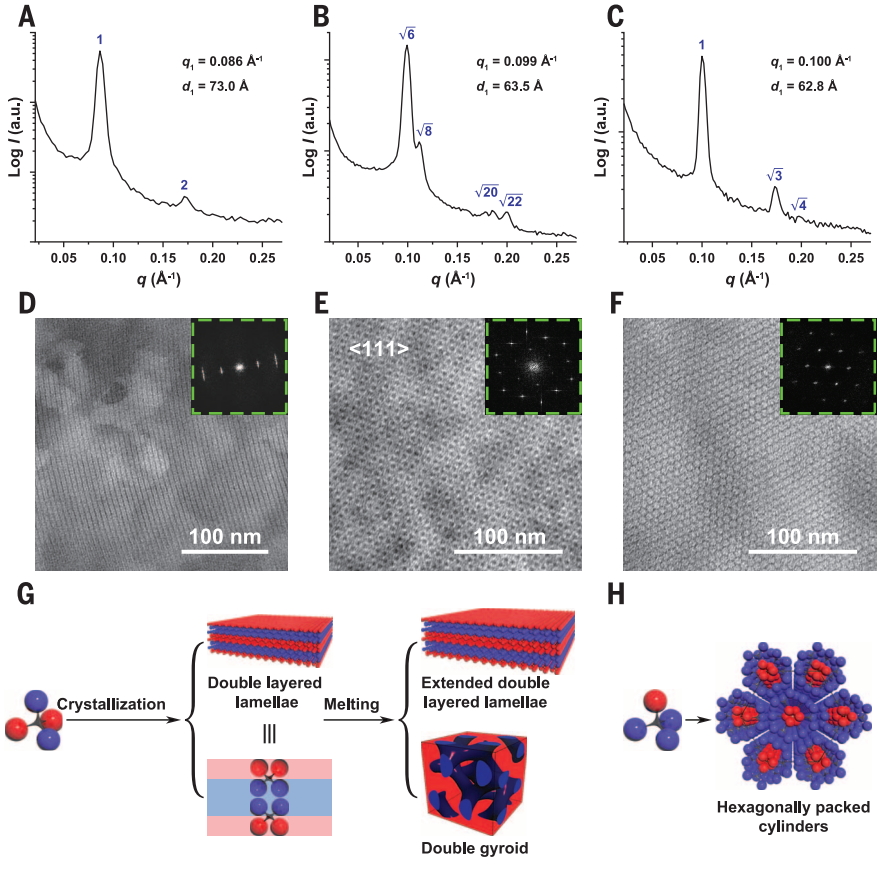

Fig. 4. Selectively assembled structures from giant tetrahedra 3 and 4. (**A** to **C**) SAXS patterns of **3c** (A), **3a** (B), and **4b** (C) were taken at 25°C after corresponding thermal treatments. (**D**) BF TEM image of thin-sectioned **3c** confirms the lamellar lattice deduced from the SAXS result shown in (A). (**E**) BF TEM image of thin-sectioned and RuO_4-stained **3a** confirms the double-gyroid lattice deduced from the SAXS result shown in (B). (**F**) BF TEM image of thin-sectioned **4b** confirms the honeycomb-like hexagonal lattice deduced from the SAXS result shown in (C). In (D) to (F), the insets are the FFT patterns of the TEM images. (**G**) Schematic illustration of the selective assembly mechanisms and packing models of **3a** to **3c**. (**H**) Schematic packing models of **4a** to **4c**.

such a double-gyroid phase from the rigid and symmetric giant tetrahedron **3a** reflects the ubiquity of the gyroid structure, implying the subtle influence of the slightly different volume fractions and interactions on the selective assembly of these giant tetrahedra (Fig. 4G).

Giant tetrahedra **4a** to **4c** failed to crystallize in similar solvent evaporation processes because of the low volume fraction of BPOSS cages that does not favor the formation of continuous 2D flat crystals (fig. S8). At such a volume fraction, an inverse spherical phase such as bcc or A15 was expected. However, after thermal annealing at 130°C, only ordered hexagonal cylinder phases were observed in **4a** to **4c**, as revealed by the q value ratio of $1:\sqrt{3}:\sqrt{4}$ in their SAXS patterns (fig. S8B, Fig. 4C, and fig. S8C for **4a**, **4b**, and **4c**, respectively) and the honeycomb-like hexagonal structure observed in BF TEM images (Fig. 4F). In the proposed schematic packing model of **4a** to **4c** (Fig. 4H), BPOSS cages are wrapped into centers of the columns while hydrophilic POSS cages with strong collective hydrogen bonding form the continuous matrix. In sharp contrast to the packing of **2a** to **2c** at higher temperatures, **4a** to **4c** tend to maximize the contacts of hydrophilic POSS cages (and thus the extent of collective hydrogen-bonding formation), which substantially minimizes the overall free energy of the system.

Symmetry breaking on accurately controlled positional interactions of nanosized giant tetrahedra has been used to construct the Frank-Kasper A15 phase and other ordered supramolecular lattices. The diverse self-assembly behaviors of these giant tetrahedra reveal that rigid, single-component soft-matter systems offer potential for building supramolecular "metal alloy analogs." The subtle competition between the persistent molecular geometry and the deformability driven by interaction terms dictates the selective assembly of the giant tetrahedra. Because of the "click" synthesis, this system is highly tunable in terms of core structure, nanoparticle functionality, and feature size. The concepts and formation mechanisms of these supramolecular structures could be extended to other giant-polyhedra molecules with different topologies and chemical compositions.

REFERENCES AND NOTES

1. M. D. Graef, M. E. Mchenry, *Structure of Materials: An Introduction to Crystallography, Diffraction and Symmetry* (Cambridge Univ. Press, Cambridge, ed. 2, 2012).
2. F. C. Frank, J. S. Kasper, *Acta Crystallogr.* **11**, 184–190 (1958).
3. F. C. Frank, J. S. Kasper, *Acta Crystallogr.* **12**, 483–499 (1959).
4. G. Ungar, X. Zeng, *Soft Matter* **1**, 95–106 (2005).
5. V. S. K. Balagurusamy, G. Ungar, V. Percec, G. Johansson, *J. Am. Chem. Soc.* **119**, 1539–1555 (1997).
6. X. Zeng *et al.*, *Nature* **428**, 157–160 (2004).
7. S. D. Hudson *et al.*, *Science* **278**, 449–452 (1997).
8. G. Ungar, Y. Liu, X. Zeng, V. Percec, W. D. Cho, *Science* **299**, 1208–1211 (2003).
9. K. Hayashida, T. Dotera, A. Takano, Y. Matsushita, *Phys. Rev. Lett.* **98**, 195502 (2007).
10. J. Zhang, F. S. Bates, *J. Am. Chem. Soc.* **134**, 7636–7639 (2012).
11. S. Lee, M. J. Bluemle, F. S. Bates, *Science* **330**, 349–353 (2010).
12. S. Lee, C. Leighton, F. S. Bates, *Proc. Natl. Acad. Sci. U.S.A.* **111**, 17723–17731 (2014).
13. S. Fischer *et al.*, *Proc. Natl. Acad. Sci. U.S.A.* **108**, 1810–1814 (2011).
14. D. V. Talapin *et al.*, *Nature* **461**, 964–967 (2009).
15. C. Xiao, N. Fujita, K. Miyasaka, Y. Sakamoto, O. Terasaki, *Nature* **487**, 349–353 (2012).
16. C. R. Iacovella, A. S. Keys, S. C. Glotzer, *Proc. Natl. Acad. Sci. U.S.A.* **108**, 20935–20940 (2011).
17. P. Ziherl, R. D. Kamien, *J. Phys. Chem. B* **105**, 10147–10158 (2001).
18. G. M. Grason, B. A. DiDonna, R. D. Kamien, *Phys. Rev. Lett.* **91**, 058304 (2003).
19. P. F. Damasceno, M. Engel, S. C. Glotzer, *Science* **337**, 453–457 (2012).
20. A. Haji-Akbari *et al.*, *Nature* **462**, 773–777 (2009).
21. D. B. Cordes, P. D. Lickiss, F. Rataboul, *Chem. Rev.* **110**, 2081–2173 (2010).
22. X. Yu *et al.*, *J. Am. Chem. Soc.* **134**, 7780–7787 (2012).
23. A. Dolbecq, E. Dumas, C. R. Mayer, P. Mialane, *Chem. Rev.* **110**, 6009–6048 (2010).
24. Y.-T. Lai, D. Cascio, T. O. Yeates, *Science* **336**, 1129 (2012).
25. W.-B. Zhang *et al.*, *Macromolecules* **47**, 1221–1239 (2014).
26. X. Yu *et al.*, *Proc. Natl. Acad. Sci. U.S.A.* **110**, 10078–10083 (2013).
27. K. Yue *et al.*, *Macromolecules* **45**, 8126–8134 (2012).
28. See supplementary materials on *Science* Online.
29. A. R. Bassindale *et al.*, *Dalton Trans.* **2003**, 2945–2949 (2003).
30. H. Liu *et al.*, *J. Am. Chem. Soc.* **136**, 10691–10699 (2014).
31. P. Ziherl, R. D. Kamien, *Phys. Rev. Lett.* **85**, 3528–3531 (2000).
32. D. Weaire, R. Phelan, *Philos. Mag. Lett.* **69**, 107–110 (1994).
33. V. Percec *et al.*, *J. Am. Chem. Soc.* **130**, 13079–13094 (2008).
34. Y. Li *et al.*, *J. Am. Chem. Soc.* **133**, 10712–10715 (2011).

ACKNOWLEDGMENTS

Supported by NSF grant DMR-1408872. We thank B. Lotz for helpful discussion. The MALDI-TOF MS analysis was assisted by K. Guo, C. Shi, and C. Wesdemiotis. Use of the Advanced Photon Source at Argonne National Laboratory was supported by the U.S. Department of Energy, Office of Science, Office of Basic Energy Sciences, under contract DE-AC02-06CH11357.

SUPPLEMENTARY MATERIALS

www.sciencemag.org/content/348/6233/424/suppl/DC1
Materials and Methods
Supplementary Text
Figs. S1 to S8
Table S1
References (*35*–*38*)

5 November 2014; accepted 2 March 2015
10.1126/science.aaa2421

METHANE CYCLING

Nonequilibrium clumped isotope signals in microbial methane

David T. Wang,[1,2] Danielle S. Gruen,[1,2] Barbara Sherwood Lollar,[3] Kai-Uwe Hinrichs,[4] Lucy C. Stewart,[5] James F. Holden,[5] Alexander N. Hristov,[6] John W. Pohlman,[7] Penny L. Morrill,[8] Martin Könneke,[4] Kyle B. Delwiche,[9] Eoghan P. Reeves,[1] Chelsea N. Sutcliffe,[3] Daniel J. Ritter,[10] Jeffrey S. Seewald,[2] Jennifer C. McIntosh,[10] Harold F. Hemond,[9] Michael D. Kubo,[11] Dawn Cardace,[12] Tori M. Hoehler,[11] Shuhei Ono[1]*

Methane is a key component in the global carbon cycle, with a wide range of anthropogenic and natural sources. Although isotopic compositions of methane have traditionally aided source identification, the abundance of its multiply substituted "clumped" isotopologues (for example, $^{13}CH_3D$) has recently emerged as a proxy for determining methane-formation temperatures. However, the effect of biological processes on methane's clumped isotopologue signature is poorly constrained. We show that methanogenesis proceeding at relatively high rates in cattle, surface environments, and laboratory cultures exerts kinetic control on $^{13}CH_3D$ abundances and results in anomalously elevated formation-temperature estimates. We demonstrate quantitatively that H_2 availability accounts for this effect. Clumped methane thermometry can therefore provide constraints on the generation of methane in diverse settings, including continental serpentinization sites and ancient, deep groundwaters.

Carbon ($^{13}C/^{12}C$) and hydrogen (D/H) isotope ratios of methane are widely applied for distinguishing microbial from thermogenic methane in the environment (*1*–*7*), as well as for apportioning pathways of microbial methane production (*8*–*10*). This bulk isotope approach, however, is largely based on empirical observations, and different origins of methane often yield overlapping characteristic isotope signals (*3*, *7*, *11*–*13*). Beyond conventional bulk isotope ratios, it has become possible to precisely measure the abundance of multiply substituted "clumped" isotopologues (e.g., $^{13}CH_3D$) (*14*, *15*). In particular, the abundance of clumped isotopes makes it possible to obtain information about the temperature at which C–H bonds were formed or last equilibrated (*14*) (fig. S1). Formation temperatures of both thermogenic and microbial methane in natural gas reservoirs can be estimated on the basis of clumped isotopologues (*16*). The mechanisms by which isotopologues attain distributions consistent with thermodynamic equilibrium, however, remain unclear because bulk methane isotopes ($\delta^{13}C$ and δD) often reflect kinetic isotope fractionations (*13*, *17*), and H isotope exchange between methane and water is sluggish (*18*).

To test whether clumped methane thermometry can be widely applied for methane sources beyond natural gas reservoirs, we examined

Editor's Summary

Creating unusual nanostructures

Self-assembly often occurs when dissimilar molecular fragments are forced together by covalent bonding. Surfactants or block copolymers are two common examples. Huang *et al.* grafted four different nanoparticles, based on polyhedral oligomeric silsesquioxanes with slightly different compositions, onto a single tetrahedal core (see the Perspective by Yang). Depending on the type of nanoparticle, they assembled into a range of defined, ordered supramolecular lattices similar to a range of metal alloys. These include phases that have higher coordination numbers than usually found in the packing of spherical objects.

Science, this issue p. 424; see also p. 396